DIRECT-HIP ALUMINIUM MATRIX COMPOSITES FOR LIGHTWEIGHT STRUCTURAL ROTORCRAFT COMPONENT PERFORMANCE AND SUPPLY CHAIN EFFICIENCY

Peter Lewis, Materion UK Ltd, Farnborough, United Kingdom
Andrew Tarrant, Materion UK Ltd, Farnborough, United Kingdom
Dr. Stefan Surrey, Materion Brush GmbH, Stuttgart, Germany
Dr. Andreas Frehn, Materion Brush GmbH, Stuttgart, Germany
Xinyi Hao, Imperial College London, London, United Kingdom
Dr. Daniel Foster, The European Synchrotron Facility, Grenoble, France
Dr. Alexander Rack, The European Synchrotron Facility, Grenoble, France
Prof. Milo Shaffer, Imperial College London, London, United Kingdom
Dr. Qianqian Li, Imperial College London, London, United Kingdom
Ash Robson, Materion UK Ltd, Farnborough, United Kingdom
Dr. Björn Reetz, Materion Brush GmbH, Stuttgart, Germany

Abstract

This paper investigates the performance and manufacturing of aluminium metal matrix composites (MMCs) reinforced with silicon carbide (SiC) for lightweight rotorcraft and aerospace structural components. New data is presented on MMC grade 2009/SiC/15p, produced via powder metallurgy and direct hot isostatic pressing (HIP). Topics evaluated include fatigue behaviour, formability and microstructural characteristics. Results demonstrate that powder metallurgy MMCs offer up to twice the high-cycle fatigue of the highest strength conventional aluminium alloys, with only minor reductions in performance for direct-HIP forms compared to the HIP+forged condition. Advanced characterisation, including synchrotron X-ray tomography, confirmed homogenous microstructure and structural stability under elevated temperature. Compression testing indicated hot formability comparable to conventional 2000-series aluminium alloys, enabling forging, extrusion or rolling where needed. Finally, recent advancements in near net shape (NNS) HIP processing highlight significant opportunities to improve material buy-to-fly ratios and streamline raw material supply chains. These findings position MMCs as a promising solution for weight reduction and performance optimisation in rotorcraft and aerospace applications.

1. NOTATION

Acronyms:

AA	Aluminium Alloy
AF	Axial Fatigue
APS	Advanced Photon Source
BSD	Backscattered Electron Detector
CTE	Coefficient of Thermal Expansion
EBSD	Electron Backscatter Diffraction
EDX	Energy Dispersive X-ray Spectroscopy
ESRF	European Synchrotron Radiation Facility
L	Longitudinal
LT	Long Transverse
MMC	Metal Matrix Composite
NNS	Near Net Shape
PCT	Phase Contrast Tomography
PMC	Polymer Matrix Composite
PPM	Parts Per Million
PS	Proof Strength
RBF	Rotating Bend Fatigue
SE	Secondary Electron
SEM	Scanning Electron Microscopy
SiC	Silicon Carbide
UTS	Ultimate Tensile Strength

2. INTRODUCTION

With the ever-increasing emphasis on net zero and sustainable aviation goals, lightweight components and associated materials selection continues to be a pivotal area. This is a critical topic in the optimisation of existing and the conception of future rotorcraft platforms. A significant expansion to existing application areas for the family of light metals can be realised through the application of innovative MMC materials. A wide variety of MMC materials based on aluminium, magnesium and titanium matrix systems are possible, however Al matrix MMCs represent the most mature of these technologies in terms of manufacturing scale and real-world applications.

Reinforcement of aluminium alloys with ultrafine ceramic particles can produce MMCs with enhanced properties, beyond what is possible with conventional lightweight metals and alloys. Such MMCs can provide solutions for lightweight rotorcraft structures due to their high specific stiffness, high cycle fatigue endurance limit, elevated temperature strength, wear resistance and low CTE. For many metallic rotorcraft components, high cycle fatigue endurance limit is a key material characteristic influencing component design and life. Most notably, Laillet (Ref. 1) previously presented the benefits of AA2009/SiC/15p MMC for structural rotorcraft components and experience for helicopter applications.

Lightweighting of structures becomes even more relevant when considering possible future use of electrical batteries and/or hydrogen fuel cells for aircraft. These technologies contribute additional weight which must be saved for somewhere else in the design. A detailed review of such challenges has been completed by Katalenich and Jacobson (Ref. 2). Lightweight materials, such as MMCs, can therefore be a key enabler of sustainable aviation goals.

Manufacture of MMCs via a powder metallurgy route utilising a novel high-energy mixing process has been shown to ensure a homogeneous reinforcement distribution. This enables a refined grain structure and isotropic mechanical and physical properties as discussed by Hashiguchi et al. (Refs. 3, 4). A summary of this manufacturing process is given by Figure 1. Using this powder metallurgy route, AA2009 has been reinforced with 15 vol.% F1000 SiC particles – 2009/SiC/15p (5 µm) and AA2124 has been reinforced with 25 vol.% F1200 SiC particles – 2124A/SiC/25p (3 µm). These MMCs have the trade names, SupremEX® 215XK and SupremEX 225XE respectively. Typical properties in the direct-HIP form are listed in Table 1. It should be noted that AMS specifications are in place, covering a range of specific grades and product forms.

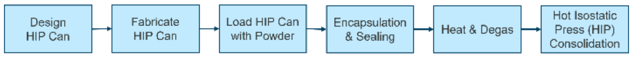

Figure 1: Schematic summary of the major steps to consolidate MMC powders by the HIP process.

Table 1: Key typical properties of the studied MMCs in the direct-HIP condition with T4 heat treatment.

Property	2009/SiC/15p (5 µm)	2124A/SiC/25p (3 µm)
Density	2.84 g/cm^3	2.88 g/cm^3
Elastic Modulus	94 GPa	115 GPa
CTE (RT-50°C)	18 ppm/°C	16 ppm/°C
0.2% PS	410 MPa	470 MPa
UTS	545 MPa	570 MPa
Strain to Failure	5%	1.8%

Characterisations by Hashiguchi et al. (Ref. 4), Winter et al. (Ref. 5) and Xia et al. (Ref. 6) have described the high fatigue performance of these MMC materials. The studies of Umer et al. (Ref. 7) showed that these MMCs can be machined via conventional high-throughput techniques. Additional property characterisations have included creep by Greasley (Ref. 8) and Roebuck et al. (Ref. 9), as well as dynamic high-strain rate impact behaviour by Li et al. (Ref. 10). Most recently, Frehn et al. (Ref. 11) investigated susceptibility to hydrogen embrittlement at ambient and elevated temperatures.

Many of the above benefits of MMCs are analogous to that of PMCs such as carbon-fibre reinforced thermoplastics, including high strength and elastic modulus. A core advantage of these MMCs is that they are fully isotropic in the direct-HIP form whilst PMCs are generally highly anisotropic due to their reliance of fibre reinforcement. Although fibre reinforced composites can provide excellent properties in the direction of reinforcement, they exhibit much lower performance in the transverse directions. In contrast, the MMCs display isotropic properties, stemming from the particle reinforcement and the HIP process used in the manufacture. Additionally, MMCs provide higher temperature capability and electrical/thermal conductivity over PMCs, whilst being non-flammable and non-outgassing.

The key prior publications on MMC materials, their applications in rotorcraft, and the content of the proposed paper are summarised by Figure 2. This paper builds upon these prior publications by introducing new materials property data, considering new test conditions, and microstructural analysis. This is complimented by high-resolution synchrotron X-ray tomography, with associated tailored image processing and analysis workflows for 3D microstructure assessment. Background on synchrotron X-ray tomography and its prior application to MMCs is given in Appendix A. Finally, manufacturing capability for NNS direct-HIP MMC forms for improved supply chain efficiency is summarised.

3. MATERIALS & METHODS

3.1. Materials

In this study, samples of Materion's commercially available SupremEX 215XK (2009/SiC/15p) MMC, in both direct-HIP and forged plate forms, were investigated. The powder metallurgy and HIP manufacturing route for these MMCs is described in Ref. 4. For direct-HIP forms, samples were extracted directly from HIP billets. As Ref. 3 outlines, the properties of these materials in the direct-HIP form are isotropic and not affected by the size or shape of a billet. However, samples were tested in both the L- and radial directions.

In the case of the forged plate samples; cylindrical HIP billets approximately Ø120 mm x 140 mm in size were forged through their diameter to achieve flat plates of approximately 25 mm thickness. Samples were subsequently extracted in the L- and LT-directions. All of the samples tested were solid-solution treated at a nominal temperature 505°C for 1 hour and subsequently quenched in cold water. Samples were then naturally aged at room temperature for ≥100 hours to achieve a T4 heat treatment. Previously generated data on the 2124A/SiC/25p MMC in equivalent product forms and test conditions is included alongside the results for comparison.

3.2. Mechanical Testing

High cycle fatigue tests were performed according to the parameters given by Table 2. AF loading ratios of R = 0.1, 0.5 and -1 were tested, with endurance limit run-out criteria set at up to $2x10^7$ cycles (approx. 140 hr testing time). In contrast, RBF tests were only completed at a loading ratio of R = -1, but with endurance limit run-out criteria set at up to $8.5x10^7$ cycles (approx. 510 hr testing time).

Table 2: Fatigue test parameters.

Characteristic	Axial (AF)	Rotating Bend (RBF)
Test Standard	ASTM E466	N/A[a]
Nominal Diameter	6.00 mm	3.81 mm
Waveform	Sinusoidal	Sinusoidal
Frequency	40Hz	47Hz
Lab Environment	Air	Air

[a]Tested according to Materion internal method

For all fractured AF specimens, fracture surface analysis was completed using an EVO Cam II HD Digital Microscope (Vision Engineering, UK).

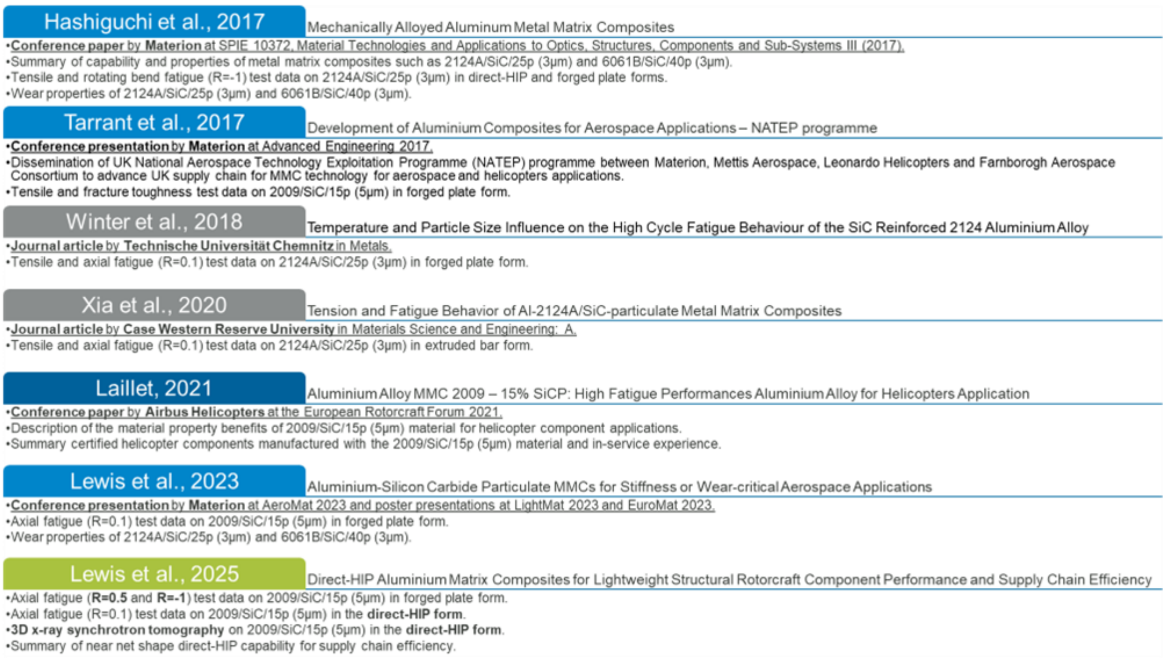

Figure 2: Summary of key prior publications and content of this paper.

Compression tests to determine flow stresses for hot forming processes (forging, rolling etc.) were completed across a 350-500°C temperature range, at strain rates of 0.1 s^{-1} and 1 s^{-1}. The tests were carried out using a continuous cylinder compression machine on a servo-hydraulic test system. To reduce friction between the specimen and compression plates, which could obstruct material flow and cause specimen bulging, a graphite-oil mixture was applied as a lubricant. Force-displacement data was recorded throughout the tests, and during the calculation of the flow curves, the influence of deformation-induced heating and friction heating was excluded to ensure a more accurate representation of the behaviour at the intended test temperatures. This approach allowed the analysis to track the response of the material under the actual furnace-set temperatures. In-line with methods described by Silk (Ref. 12), the compressive flow stress values at 0.1% strain were used to assess the combined effect of temperature and strain rate on flow stress.

3.3. Microstructural Analysis

Optical microstructural analysis was completed using a Zeiss AxioLab5 optical microscope equipped with ZEN core imaging software (Zeiss, Germany). Additionally microstructural analysis was completed using SEM and EDX. Samples for SEM analyses were initially ground using 600, 1200, and 2500-grit SiC sandpaper with water as a lubricant. The final grinding was performed using 4000-grit sandpaper lubricated with ethanol. The polishing process was carried out with primary polishing by 1 μm oil-based diamond suspension and secondary polishing with the mixture of OPS and isopropanol (1:1). Before SEM, ion milling was used to remove the oxide layer on Al. The SEM was then conducted using a Zeiss Sigma-300 SEM (Zeiss, Germany). The phase distributions were examined using BSD and SE modes. To identify the phases within the composite EDX spectroscopy (Bruker, Germany) and EBSD were employed. The EBSD analysis was performed using Bruker eFlash detector (Bruker, Germany) equipped in Zeiss Sigma-300 SEM.

X-ray synchrotron tomography was performed on ESRF ID19 beamline under project MA-6398. For this analysis, a sample of 2009/SiC/15p MMC in the direct-HIP form with T4 heat treatment was used. The scanned area was a cylinder with a diameter of 500 μm and a height of 500 μm. The sample was exposed to elevated temperature of 190°C, with in-situ imaging at 1-hour intervals to assess stability of the microstructure at elevated temperature operating conditions. To fit into the field of view of the X-PCT setup, the samples were lathe machined and ground with 2500-grit sandpaper, into rods of 500 μm in diameter and 700 μm in height and then fixed on an alumina rod (Ø2 mm), as in Figure 3. The X-ray synchrotron tomography was performed on ESRF ID19 beamline. PCT was performed at an X-ray energy of 26.1 keV with a propagation distance of 10 mm between the sample and the detector. A x20 optical objective lens (0.75 numerical aperture) lens-coupled a single-crystal scintillator (LSO:Tb, 2 micrometer thin) to a pco.edge sCMOS based camera, type 5.5, resulting in an effective pixel size of 0.31 μm and a resolution of 2560 x 2160 pixels. The detector was positioned 12 mm downstream of the sample to benefit from propagation-based X-ray phase contrast. 4000 projections were collected over 360º with an exposure time of 100 ms per projection. 50 dark images and 2 sets of 101 flat field images were used to correct, respectively, for the dark current of the camera and beam inhomogeneities. The tomography datasets were reconstructed using Tomwer with and without prior phase-retrieval (Paganin approach, delta/beta ratio of 10).

Figure 3: Measurement set up at ID19, the ESRF.

4. RESULTS & DISCUSSION

4.1. Fatigue

The AF data generated with R-ratio of 0.1 is given by Figure 4 for both direct-HIP and forged forms. In addition, AF data at R-ratio of 0.5 is presented by Figure 5. Extensive testing at R-ratio of -1 has completed using both AF and RBF loading conditions across product forms, as shown in Figure 6. Here, a good correlation between the AF and RBF test data is shown.

Comparing the two datasets for 2009/SiC/15p in Figure 4, the forged plate condition can be seen to show a fatigue limit of around 50 MPa (~16%) greater than that of the direct-HIP condition.

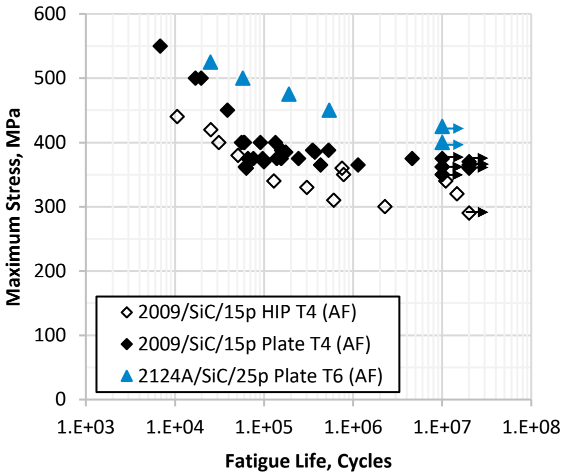

Figure 4: Unnotched R=0.1, room temp fatigue data. Arrows indicate test endurance limit was reached.

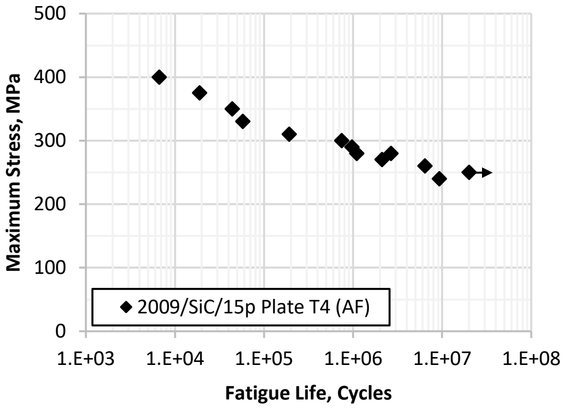

Figure 5: Unnotched R=0.5, room temp fatigue data. Arrows indicate test endurance limit was reached.

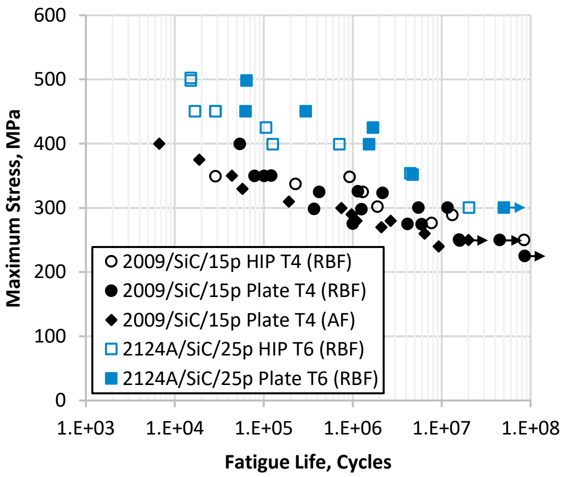

Figure 6: Unnotched R=-1, room temp fatigue data. Arrows indicate test endurance limit was reached.

It would appear that the AF test is more sensitive to detect this difference in performance between product forms. Although the RBF data in Figure 6, displays a difference in fatigue limit between product forms, it is less clear than in AF shown in Figure 4. In RBF, cracks often initiate at the surface where the stress is highest, while in AF, cracks can initiate at various points due to the uniform stress distribution. Thus, in AF a larger volume of material is tested, making it a more sensitive test in terms of detecting differences in fatigue performance between product forms as indicated by results of Figure 4 and Figure 6.

Overall, the MMCs tested show much greater high-cycle fatigue limits than commonly used high-strength aluminium alloys such as AA2024 and AA7075. Additionally, even higher fatigue limits for these MMC materials have been reported for extruded bar materials by Xia et al. (Ref. 6). The high cycle fatigue strength at 10^7 cycles, determined by axial fatigue test, of the MMCs is listed in Table 3. Based on these results, it can be deduced that the MMCs tested offer an increase in fatigue strength of up to 2 times the highest strength aluminium alloys, with negligible change in density. Similar results have been reported by Laillet (Ref. 1), where MMC fatigue limits "*2 to 3 times higher than on conventional Al alloys*" were stated.

The high fatigue performance of these MMCs is a result of their highly refined grain structure, inherent from the reinforcement with ultrafine SiC particles. It is understood from the work of Lewandowski et al. (Ref. 6 and Ref. 13) that this is due to the interaction of the aluminium alloy matrix with higher modulus SiC particulate and strain rate hardening lead to this improved MMC fatigue strength. The SiC particles effectively pin dislocation movement and hinder crack propagation, increasing the stress required to initiate and grow fatigue cracks, particularly in the high cycle regime. Additionally, the high elastic modulus of the MMCs leads to reduced strain at a given stress level, further enhancing fatigue resistance. These effects result in the MMCs having an extremely high fatigue limit relative to their yield strength, as well as a much harder fatigue limit than is typical for conventional aluminium alloys. In addition, the S-N curves presented in Figure 4 to 6 also show a low degree of scatter in fatigue life for any given stress level.

Table 3: Summary of unnotched room temperature axial fatigue data on the MMCs tested.

Material	Product Form	Orientation	Heat Treatment	R-ratio	Fatigue Limit (10^7 cycles), MPa	Density, g/cm^3	Elastic Modulus, GPa
2009/SiC/15p	HIP	All	T4	0.1	316	2.84	94
2009/SiC/15p	Plate	L & LT	T4	0.1	367	2.84	94
2124A/SiC/25p	Plate	L & LT	T6	0.1	425	2.88	115
2124A/SiC/25p	Rod/Bar	L	T4	0.1	448[a]	2.88	115
2009/SiC/15p	Plate	L & LT	T4	0.5	411	2.84	94
2009/SiC/15p	Plate	L & LT	T4	-1	240	2.84	94

[a]Result from Ref. 5

For all product forms and test conditions, 2124A/SiC/25p shows greater fatigue performance than 2009/SiC/15p. This is in-line with static strength and elastic modulus, and is due to the higher loading, and finer size of SiC particulate. Whilst 2124A/SiC/25p offers higher elastic modulus and strength than 2009/SiC/15p, a key benefit of the 2009/SiC/15p is the ductility (5-8% typical, depending on product form) and fracture toughness (28 MPa√m typical) being more comparable to that of common aluminium alloys. As such, 2009/SiC/15p can in many cases offer a more balanced set of properties for damage tolerant aerospace and rotorcraft component designs.

Although the relative increase in fatigue limit that the 2009/SiC/15p MMC has been shown to provide over conventional high-strength aluminium alloys is significant for R = -1 and R = 0.1, it appears to be less substantial at R = 0 .5. It can therefore be said these MMCs provide maximum benefit, in terms of fatigue performance, when the stress amplitude is high. The rationale for this effect could provide an interesting area for further study alongside testing of additional MMC compositions and product forms at R = 0.5.

Considering the specific fatigue limit (fatigue limit-to-density ratio) it can be said that these MMCs have comparable performance to that of Ti-6Al-4V and other titanium alloys. At the same time, they provide improvement in specific stiffness (elastic modulus-to-density ratio), as Figure 7 illustrates. From this perspective, when lightweight, fatigue resistance is needed, powder metallurgy MMCs are an obvious choice; particularly if the properties of elastic modulus and wear resistance are also relevant for the application. As discussed by Laillet et al. (Ref. 1) the combination of fatigue and wear, and the so-called "fretting fatigue" property, can be a key design characteristic for rotorcraft components.

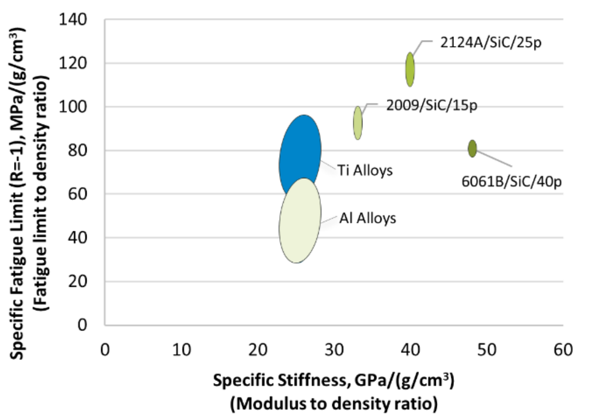

Figure 7: Specific fatigue limit (R = -1) versus specific stiffness comparison between materials.

4.2. Fracture Surface Analysis

AF coupon fracture surface images, for each product form and test condition are found in Figure 8 to Figure 11. In all cases, a fatigue fracture surface typical of a metal is observed, with a clear initiation zone indicated by "beach mark" effects and a smooth, brighter area at the edge of each specimen. This highlights that these MMCs fail like a metal, with the fracture occurring through the ductile matrix or at the matrix-particle interface, but not through the SiC particle reinforcement.

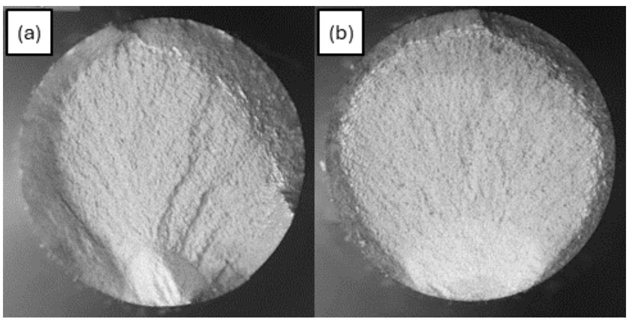

Figure 8: R=0.1 forged plate 2009/SiC/15p axial fatigue fracture surfaces for coupons failing at (a) 1.7×10^4 cycles, and (b) 4.3×10^6 cycles.

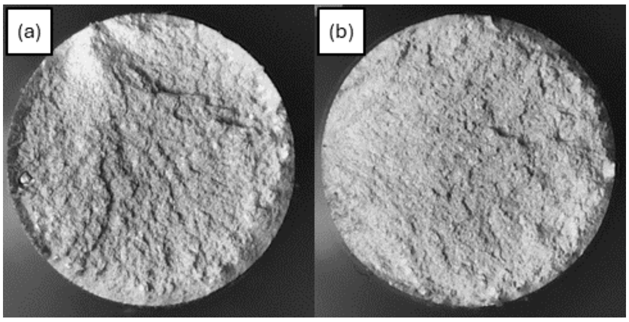

Figure 9: R=0.1 direct-HIP 2009/SiC/15p axial fatigue fracture surfaces for coupons failing at (a) 1.1x10^4 cycles, and (b) 2.3x10^6 cycles.

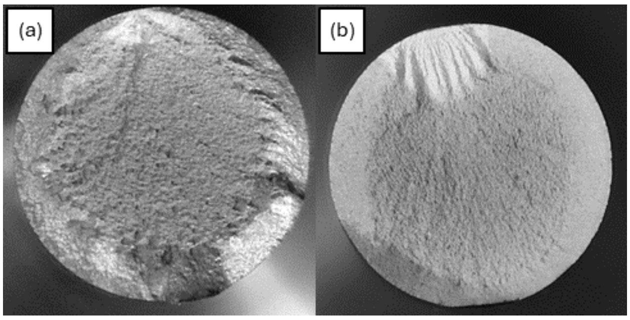

Figure 10: R=0.5 forged plate 2009/SiC/15p axial fatigue fracture surfaces for coupons failing at (a) 2.2x10^4 cycles, and (b) 1.3x10^6 cycles.

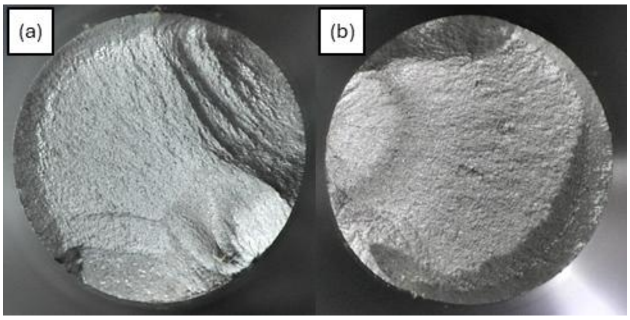

Figure 11: R=-1 forged plate 2009/SiC/15p axial fatigue fracture surfaces for coupons failing at (a) 5.7x10^4 cycles, and (b) 6.4x10^6 cycles

Within each figure a lower cycle (<10^5) and higher cycle (>10^6) failure example is given. The initiation and propagation zones are generally larger in size for the higher cycle regime failures, coupled with a smoother, more ductile, final fracture zone for the higher cycle failure regimes.

Examining the fracture surfaces of the direct-HIP material in Figure 9, coarser fracture surfaces are observed in comparison to equivalent forged samples. This may be linked to the slightly lower fatigue limits determined for the direct-HIP condition, and/or is an artefact of changes to grain structure from hot working. It should be noted however, that the forged plate tests were conducted in the L- and LT- directions. It may be that fatigue life and fracture mechanics in the ST direction may align more with that of the direct-HIP condition. Due to the forged plate materials used in this study being only 25 mm it was not possible to complete mechanical testing in the ST- direction. This could be an interesting topic for future characterisation of thicker product forms.

4.3. Compressive Flow Stress

Compression testing data is presented as peak flow stress versus temperature for a strain rate of 0.1 s^{-1} in Figure 12 and 1 s^{-1} in Figure 13. At typical hot working temperatures for aluminium alloys (400-500°C), the MMCs show similar or slightly lower compressive flow stresses. Although the minor differences seen here are not necessarily statistically significant, it does provide a strong indication that these powder metallurgy MMCs are similarly formable as conventional 2000-series aluminium alloys. This demonstrates that these materials can be readily hot forged, extruded or rolled, where required.

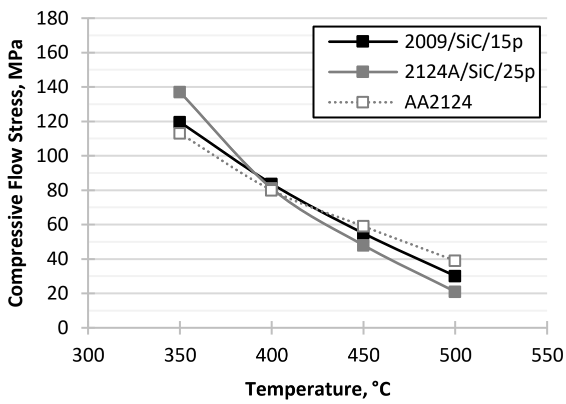

Figure 12: Temperature dependence of compressive flow stress at 0.1s^{-1} strain rate.

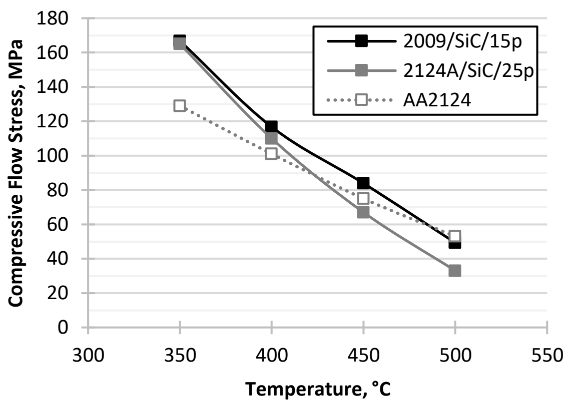

Figure 13: Temperature dependence of compressive flow stress at 1s^{-1} strain rate.

4.4. Microstructure

An ultrafine isotropic microstructure with homogenous distribution of SiC particulate within the aluminium alloy matrix was observed for all materials tested. Example optical micrographs are given by Figure 14 and Figure 15 for the 2009/SiC/15p and 2124A/SiC/25p MMCs respectively.

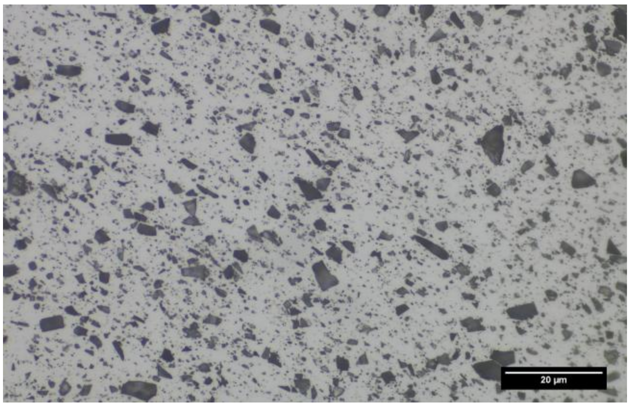

Figure 14: Optical micrograph of 2009/SiC/15p in the direct-HIP product form with T4 heat treatment.

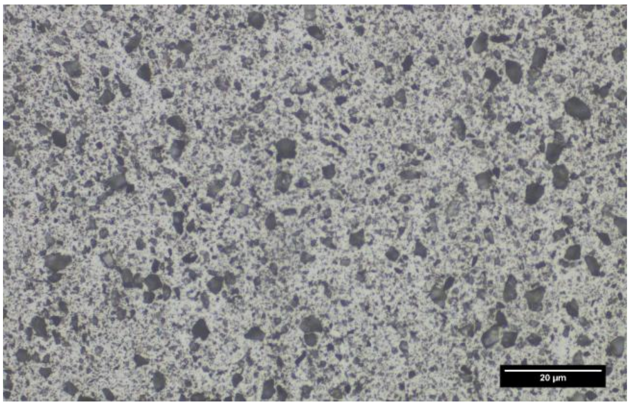

Figure 15: Optical micrograph of 2124A/SiC/25p in the direct-HIP product form with T6 heat treatment.

Figure 16 presents representative EDX mapping and point analyses of the 2009/SiC/15p MMC. This identified the key phases including the aluminium matrix, uniformly dispersed SiC reinforcement, and Cu-rich precipitation hardening phases. The SEM image also revealed a fine and uniform microstructure with no porosity, indicating successful consolidation during the HIP process.

EBSD analysis was conducted to assess the distribution and orientation of SiC particles within the MMC. As shown in Figure 17, the SiC particles are randomly oriented and well dispersed, confirming effective mixing and reinforcement uniformity. This random orientation of the SiC particles leads to the isotropic properties of the MMC material.

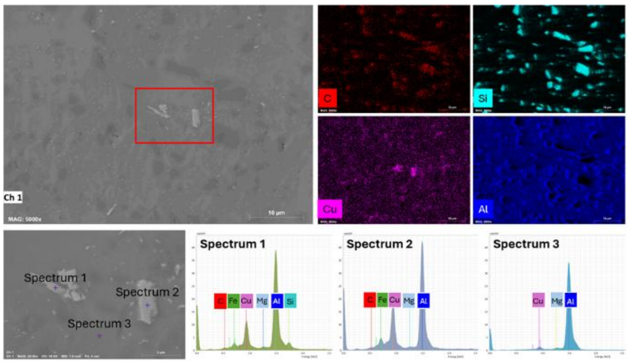

Figure 16: EDX mapping and point analysis of the general phases in 2009/SiC/15p MMC in direct-HIP form with T4 heat treatment.

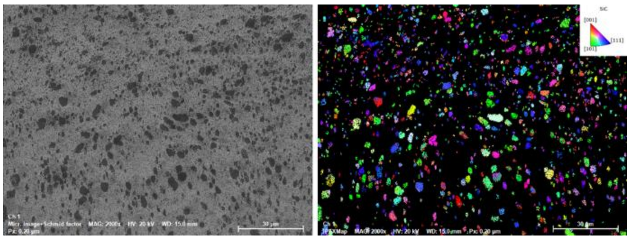

Figure 17: *EBSD of SiC within* 2009/SiC/15p MMC in direct-HIP form with T4 heat treatment.

Due to the severe plastic deformation of the aluminium matrix from powder processing, the EBSD signal from the Al grains was weak, limiting phase indexing of the matrix itself. These findings relating to SiC particles are in-line with that of Reiff-Musgrove et al. (Ref. 14), who studied 6063/SiC/20p and 6063/SiC/30p MMCs manufactured by the same powder metallurgy process. In contrast, some assessment of the matrix grain structure and texture was achieved in Ref. 19, for forged plate samples, which highlighted the fine matrix grain structure of these MMC materials.

To gain more insights into the 3D structure, synchrotron X-ray tomography was employed. Reconstructed cross-sections (Figure 18) revealed clear contrast between phases. These 3D tomography results indicate that the SiC phases are homogeneously distributed within the scanned volume. Based on volumetric analysis, the SiC content was calculated to be within 0.7 vol%, of the actual value of 15 vol%. Thus, the voxel size of 0.28 µm in this study has proven suitable for resolving the morphology and spatial distribution of SiC. This resolution allowed reliable segmentation and approximate volumetric analysis, making it a valuable tool for future in-situ or fatigue-related investigations.

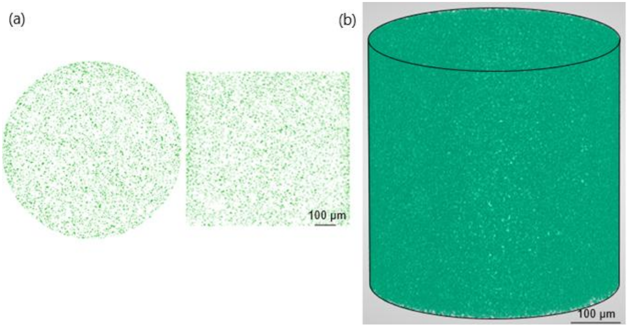

Figure 18: X-ray tomography reconstruction of 2009/SiC/15p T4 sample after 4 hours at 190°C; (a) the distribution of SiC (in green) in the cross-section and longitudinal section, (b) 3D distribution of SiC.

No changes in the SiC distribution were observed after 4 hours of 190°C heat treatment, thus highlighting the stability of the microstructure at elevated temperature. It would be expected that some coarsening of the precipitation hardening phases will occur at these temperatures, however it was not possible to fully resolve these phases at the voxel size employed. For complete 3D assessment of the microstructure, including precipitation hardening phases, a finer voxel size would need to be applied in future studies. It would be equally interesting to explore the effects of elevated temperature exposure on the mechanical properties of 2009/SiC/15p MMC. Based on the experience from Hashiguchi et al. (Refs. 3, 4) on the elevated temperature properties of 2124A/SiC/25p, it would be expected that 2009/SiC/15p also provides strong improvements in elevated temperature static and dynamic strength over conventional aluminium alloys.

5. Manufacturing

For multiple decades, powder metallurgy MMCs have been used in high-consequence applications across a range of industries, including rotorcraft. Traditionally these have been manufactured by machining from solid direct-HIP or forged blocks, or in some cases by forging or extruding to shape via complex international supply chains.

As indicated by the fatigue data presented in Section 4.1 on direct-HIP MMC forms, only a slight knockdown in performance is realised versus hot worked forms, whilst maintaining comparable benefits in terms of lightweight stiffness and fatigue performance versus conventional aluminium and titanium alloys. In recent years, significant development of near-net shape direct-HIP product forms has been achieved. Examples of the NNS direct-HIP manufacturing capability that has been successfully developed with the commercially available SupremEX MMC materials are shown in Figure 19. These direct-HIP product forms highlight an opportunity to drastically increase buy-to-fly ratios, whilst leveraging isotropic properties for design simplification. They have the potential to improve raw material supply chain efficiencies through the refinement or, in some cases, elimination of hot working steps to achieve the necessary component geometries. Such NNS-HIP approaches have proven to lead to reduced waste generation and lower energy consumption per unit mass in comparison to traditional forming methods, as explained by Kruzhanov and Arnhold (Ref. 15). In the case of powder metallurgy MMCs, this is primarily by maximizing buy-to-fly ratios through reduced raw material consumption.

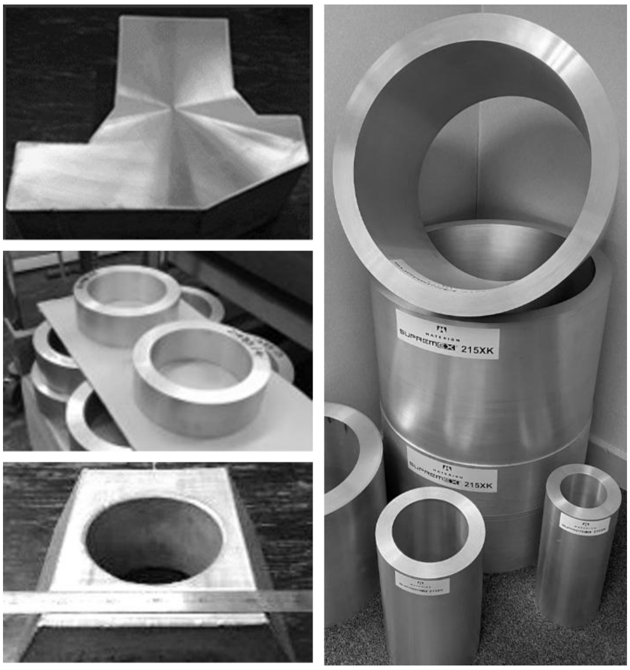
Figure 19: Examples of direct-HIP MMC forms, including tubular and near-net-shape geometries.

6. CONCLUSIONS

The most important results of this paper are summarized as follows:

1. 2009/SiC/15p and 2124A/SiC/25p MMC provide significant improvement in high-cycle fatigue limit versus conventional high-strength aluminium alloys, across R=0.1, R=0.5 and R=-1 conditions. These materials also provide a substantial increase in elastic modulus to weight ratio compared to conventional alloy systems.

2. A slight knockdown in fatigue limit is realised by using direct-HIP MMC as opposed to a hot worked form.
3. 2009/SiC/15p and 2124A/SiC/25p MMCs are comparable in terms of formability to conventional 2000-series aluminium alloys
4. Successful characterisation of 2009/SiC/15p MMC using high-resolution synchrotron X-ray tomography, enabling 3D visualisation of the microstructure at submicron resolution, revealing homogeneous SiC particle dispersion.
5. Near net shape HIP capability provides opportunity to drastically increase buy-to-fly ratios and improve raw material supply chain efficiencies through the elimination of hot working steps.

Author contact:

Peter Lewis peter.lewis@materion.com

Andrew Tarrant andrew.tarrant@materion.com

Dr. Stefan Surrey stefan.surrey@materion.com

Dr. Andreas Frehn andreas.frehn@materion.com

Xinyi Hao a.hao21@imperial.ac.uk

Dr. Daniel Foster daniel.foster@esrf.fr

Dr. Alexander Rack alexander.rack@esrf.fr

Prof. Milo Shaffer m.shaffer@imperial.ac.uk

Dr. Qianqian Li qianqian.li@imperial.ac.uk

Ash Robson ash.robson20@imperial.ac.uk

Dr. Björn Reetz Bjoern.Reetz@materion.com

7. APPENDIX A

X-ray tomography is a non-destructive imaging technique capable of providing high-resolution, three-dimensional representations of material microstructure. It is a powerful tool for investigating the relationship between 3D microstructural features and the mechanical properties of MMCs. Advanced studies in this field rely heavily on high-brightness synchrotron X-ray sources, which offer both high spatial and temporal resolution.

The application of synchrotron radiation to aluminium MMCs dates back over two decades and continues to evolve. In 2001, Babout et al. (Ref. 16) employed synchrotron X-ray tomography at the ID19 beamline of the ESRF, achieving a spatial resolution of 2 µm to examine an aluminium MMC reinforced with 40–60 µm ceramic balls. Their study included 3D reconstruction of internal porosity. In 2004, Borbély et al. (Ref. 17) used the same beamline to investigate an AA6061 matrix composite containing 20 vol.% Al_2O_3 particles, achieving a pixel size of 1.9 µm and successfully reconstructing the 3D particle distribution. Further developments were demonstrated in 2010, when de Andrade Silva et al. (Ref. 18) used the third-generation synchrotron source, BESSY in Germany, to quantify the morphology and size distribution of pores and Fe-rich inclusions in a AA2080 alloy composite reinforced with 25 µm SiC particles. In parallel, Williams et al. (Ref. 19) utilised the APS at Argonne National Laboratory to analyse damage behaviour in the same composite system, reconstructing SiC particles, matrix voids, and cracks within particles.

As tomography hardware and detector technology have advanced, temporal resolution has improved dramatically — down to acquisition times as low as 1 ms — enabling real-time, in situ studies of dynamic material behaviour. For example, in 2014, Hruby et al. (Ref. 20) conducted the first in situ X-ray tomography experiments on fatigue crack growth in SiC particle-reinforced AA2080 MMCs at the APS 2-BM beamline. In more recent work, image segmentation has been significantly improved using machine learning. Tsamos et al. (Ref. 21) applied deep convolutional neural networks to XCT datasets of aluminium MMCs reinforced with SiC particles and Al_2O_3 fibres, successfully distinguishing between fibres, intermetallic phases, silicon, SiC, and the aluminium matrix. These studies are summarised in Table A, highlighting the development composite systems and the key findings over time.

Table A: History of tomography application to MMCs.

Ref.	Beamline	Resolution (µm)	Material	Main Conclusions
[16]	ESRF ID19	2	Al MMC	Porosity characterization
[17]	ESRF ID19	1.9	AA6061 + Al_2O_3	3D mapping of Al_2O_3 particles
[18]	BESSY II BAM	3.2	AA2080 + SiC	Pores and Fe-inclusion visualization
[19]	APS 2-BM	-	AA2080 + SiC	Cracks, voids, and particle behaviour
[20]	APS 2-BM	1.47	AA2080 + SiC	In-situ crack propagation visualization
[21]	BESSY II BAM	0.44	Various Al MMCs	ML segmentation of complex microstructures

8. ACKNOWLEDGMENTS

We acknowledge the European Synchrotron Radiation Facility (ESRF) for provision of synchrotron radiation facilities under proposal MA-6398.

9. REFERENCES

1. Laillet, E., “Aluminium alloy MMC 2009 - 15% SiCP: High fatigue performances Aluminium alloy for helicopter applications,” 47th European Rotorcraft Forum, Online Only, 2021.

2. Katalenich S. M. and Jacobson, M. Z., “Towards battery electric and hydrogen fuel cell military vehicles for land, air and sea,” *Energy*, Vol. 254, 2022, pp. 124355.

3. Hashiguchi, D., Tricker, D., Tarrant, A., Campbell, J., and Pokross, C., “Discontinuously reinforced aluminum MMC extrusions,” *Metal Powder Report*, Vol. 72, (4), 2017, pp. 252-258.

4. Hashiguchi, D., Tricker, D., and Tarrant. A., “Mechanically Alloyed Aluminum Metal Matrix Composites,” SPIE 10372 Material Technologies and Applications to Optics Structures Components and Sub-Systems III, San Diego, CA, 2017.

5. Winter, L., Hockauf, K., and Lampke, T., “Temperature and Particle Size Influence on the High Cycle Fatigue Behavior of the SiC Reinforced 2124 Aluminum Alloy,” *Metals*, Vol. 8, (1), 2018, pp. 43.

6. Xia, J., Lewandowski, J. J., and Willard, M. A., “Tension and Fatigue Behavior of Al-2124A/SiC-particulate Metal Matrix Composites,” *Materials Science and Engineering: A*, Vol. 770,, 2020, pp. 138518.

7. Umer, U., Mohammed, M. K., Abidi, M. H., Alkhalefah, H., and Kishawy, H. A., “Machinability analysis and multi-response optimization using NGSA-II algorithm for particle reinforced aluminum based metal matrix composites,” *Advances in Production Engineering & Management*, Vol. 17, (2), 2022, pp. 205-218.

8. Greasley, A., “Creep of dispersion reinforced aluminium based metal matrix composite,” *Materials Science and Technology*, Vol. 11, (2), 1995, pp. 163-166.

9. Roebuck, B., Gee, M. G., Lord, J. D., and McCartney, L. N., “Miniature thermal cycling tests on aluminium alloy metal matrix composites,” *Materials Science and Technology*, vol. 14, (9-10), 1998 pp. 1001-1008.

10. Li, X., Kim, J., Roy, A., and Ayvar-Soberanis, S., “High temperature and strain-rate response of AA2124-SiC metal matrix composites,” *Materials Science and Engineering: A*, vol. 856, p. 144014, 2022.

11. Frehn, A., Krus, D., and Mack, S, “High-Performance Alloys for Conventional ICE and Hydrogen ICE Applications,” ASME 2023 ICE Forward Conference, Pittsburgh, PA, 2023.

12. Silk, J. R., “The Influence of Secondary Processing Conditions on the Mechanical Properties and Microstructure of a Particle Reinforced Aluminium Metal Matrix Composite,” Imperial College London, 2008.

13. Hassan, H. A. and Lewandowski, J. J. “Fracture Toughness and Fatigue of Particulate Metal Matrix Composites,” *Comprehensive Composite Materials II*, Vol. 4, 2018, pp. 86–136.

14. Reiff-Musgrove, R., Gaiser-Porter, M., Gu, W., Campbell, J. E., Lewis, P., Frehn, A., Tarrant, A. D., Tang, Y. T., Burley, M. and Clyne, T. W., “Indentation Plastometry of Particulate Metal Matrix Composites, Highlighting Effects of Microstructural Scale,” *Advanced Engineering Materials*, Vol. 25, 2023, pp. 2201479. DOI: 10.1002/adem.202201479.

15. V. Kruzhanov and V. Arnhold, “Energy consumption in powder metallurgical manufacturing,” *Powder Metallurgy*, Vol. 55, (1), 2012, pp. 14-21.

16. Babout, L., Maire, E., Buffière, J. Y., and Fougères, R., “Characterization by X-ray Computed Tomography of Decohesion, Porosity Growth and Coalescence in Model Metal Matrix Composites,” *Acta Materialia*, Vol. 49, (11), 2001, pp. 2055–2063. DOI: 10.1016/S1359-6454(01)00104-5.

17. Borbély, A., Csikor F. F., Zabler S., Cloetens P., Biermann H., “Three-Dimensional Characterization of the Microstructure of a Metal–Matrix Composite by Holotomography,” *Materials Science and Engineering: A*, Vol. 367, (1–2), 2004, pp. 40–50. DOI: 10.1016/j.msea.2003.09.068.

18. De Andrade Silva, Williams J. J., Müller B. R., Hentschel M. P., Portella P. D., Chawla N., “Three-Dimensional Microstructure Visualization of Porosity and Fe-Rich Inclusions in SiC Particle-Reinforced Al Alloy Matrix Composites by X-ray Synchrotron Tomography,” *Metallurgical and Materials Transactions A*, Vol. 41, (8), 2010, pp. 2121–2128. DOI: 10.1007/s11661-010-0260-0.

19. Williams, J., Flom, Z., Amell, A. A., Chawla, N., Xiao, X., and De Carlo F., “Damage Evolution in SiC Particle Reinforced Al Alloy Matrix Composites by X-ray Synchrotron Tomography,” *Acta Materialia*, Vol. 58, (18), 2010, pp. 6194–6205. DOI: 10.1016/j.actamat.2010.07.039.

20. Hruby, P., Singh S. S., Williams J. J., Xiao X., De Carlo F., Chawla N.., “Fatigue Crack Growth in SiC Particle Reinforced Al Alloy Matrix Composites at High and Low R-Ratios by In Situ X-ray Synchrotron Tomography,” *International Journal of Fatigue*, Vol. 68, 2014, pp. 136–143. DOI: 10.1016/j.ijfatigue.2014.05.010.

21. Tsamos, A., Curioni, M., Rowenhorst, D., Maire, E., Babout, L., and Withers, P. J., “Synthetic Data Generation for Automatic Segmentation of X-ray Computed Tomography Reconstructions of Complex Microstructures,” *Journal of Imaging*, Vol. 9, (2), 2023, p. 22. DOI: 10.3390/jimaging9020022.